Electronic structure of the Ru(0001) surface

Electronic structure of the Ru(0001) surface

T Pelzer†, G Ceballos†, F Zbikowski†, B Willerding†, K Wandelt†,
U Thomann‡, Ch Reuß‡, Th Fauster‡ and J Braun§

† Institute of Physical and Theoretical Chemistry, University of Bonn, Wegelerstrasse 12,
D-53115 Bonn, Germany
‡ Lehrstuhl für Festkörperphysik, University of Erlangen–Nürnberg, Staudtstrasse 7,
D-91058 Erlangen, Germany
§ Fachbereich Physik, University of Osnabrück, Barbarastrasse 7, D-49069 Osnabrück, Germany

Abstract. This paper deals with the electronic structure of ruthenium. Synchrotron radiation in the range from 15 to 45 eV and angle-resolved ultraviolet photoemission are used to map the energies of the electronic states. The Fermi surface of Ru is determined using angle-resolved ultraviolet photoemission spectroscopy. The experimental results are compared with calculated photoemission spectra obtained within the framework of the one-step model of photoemission.

1. Introduction

For a better understanding of the chemical and catalytic properties of Ru a profound knowledge of its electronic structure is needed. In the following we present measurements and calculations relating to the electronic structure in the valence band region.

The topology of the Fermi surface of ruthenium has been investigated in a direct fashion using an ellipsoidal mirror display analyser which gives two-dimensional images of the photo-electron intensity versus emission angle. The results are in excellent agreement with previous studies and provide new perspectives for Fermi surface studies.

The paper is organized as follows: the next section describes the experimental set-up, the third one gives a short description of the theory, in the fourth the Fermi surface of Ru is determined, the fifth is concerned with the bandstructure of Ru along different directions and the last one before the summary deals with the surface states of Ru(0001).

2. Experiment

The measurements were performed using photons from the TGM3 beamline at the 800 MeV storage ring BESSY in Berlin. The incoming photon flux was monitored via the photocurrent of the focusing mirror. The synchrotron radiation was linearly polarized to 90%. The overall energy resolution was 350 meV. The apparatus was described earlier [1].

For the experiments the (0001) surface of a ruthenium single crystal was used. Impurities like carbon and sulphur were removed from the surface by sputtering with an argon-ion beam of 800 eV and a current of 2 μA at a temperature of 80 K for 15 minutes. The near-surface region was then depleted as regards the remaining carbon by oxidation at 1550 K and an oxygen pressure of 10^{-5} Pa for ten minutes, alternating with heating and carbon segregation in the

absence of oxygen. Finally a dose of 10 L O_2 was applied at a temperature below 500 K and this was followed by the detection of CO and SO_2 TD spectra; that excess oxygen had been removed was ascertained by expanding the TD spectra up to 1550 K. After several such cycles, an Auger spectrum was taken to verify the complete desorption of oxygen.

The energy analyser used for the position-sensitive measurements was constructed by Rieger *et al* [1] following a concept proposed by Eastman *et al* [2]. It allows one to perform not just ARUPS (angle-resolved ultraviolet photoemission spectroscopy) but also LEED experiments.

The data were acquired with an IBM-compatible PC using a programme written by Pistitsch [3] and Thomann. The angular intensity distribution patterns taken by a CCD camera were corrected for the locally differing sensitivity of the luminescence screen by dividing the images by a reference picture recorded while the detector was uniformly illuminated [3]. The high-symmetry directions were determined from the ARUP spectra.

Ruthenium crystallizes in HCP structure with the lattice constants $a = 2.704$ Å and $c = 4.282$ Å [4]. The work function of the (0001) surface is approximately 5.52 eV [5], the melting temperature 2538 K [6].

3. Theory

A detailed description of the relativistic theory of photoemission is given elsewhere [7]. Therefore, we present here only the basic formulae of a relativistic one-step theory. In the framework of the one-step model of photoemission the spin-averaged electron current is given by the following expression:

$$I(\mathbf{k}_|, \epsilon_f) = -\frac{1}{\pi} \text{Im} \langle \mathbf{k}_\|, \epsilon_f | G_2^+ \Delta G_1^+ \Delta^+ G_2^- | \mathbf{k}_\|, \epsilon_f \rangle. \tag{1}$$

$G_2^\pm$ and G_1^+ are 4×4 matrices and represent the relativistic retarded (G^+) and advanced (G^-) single-particle Green functions for the final (G_2) and the initial state (G_1). In a relativistic theory the interaction of an electron with the electromagnetic field is described by the operator

$$\Delta = -\boldsymbol{\alpha} \cdot \boldsymbol{A}_0 \tag{2}$$

where $\boldsymbol{A}_0$ denotes the spatially constant amplitude of the electromagnetic vector potential. The three components α_k of the vector $\boldsymbol{\alpha}$ are defined through the tensor product $\alpha_k = \sigma_1 \otimes \sigma_k$, $k = 1, 2, 3$, where σ_k denote the Pauli spin matrices.

In the space representation we obtain

$$\rho = -\frac{1}{\pi} \text{Im} \int \text{d}\boldsymbol{r} \int \text{d}\boldsymbol{r}' \ \Psi_f^\dagger(\boldsymbol{r}) \Delta G_1^+(\boldsymbol{r}, \boldsymbol{r}') \Delta^\dagger \Psi_f(\boldsymbol{r}') \tag{3}$$

with the time-reversed SPLEED state

$$\Psi_f^\dagger(\boldsymbol{r}) = \langle \boldsymbol{r} | G_2^+ | \epsilon_f, \boldsymbol{k}_\| \rangle. \tag{4}$$

The spin-averaged photocurrent I follows as

$$I = \text{trace}(\rho). \tag{5}$$

As a consequence of multiple-scattering theory, the spin-density matrix is divided into four different contributions:

$$\rho(\epsilon_f, \boldsymbol{k}_\|) = \rho^{atom}(\epsilon_f, \boldsymbol{k}_\|) + \rho^{intra}(\epsilon_f, \boldsymbol{k}_\|) + \rho^{inter}(\epsilon_f, \boldsymbol{k}_\|) + \rho^{surf}(\epsilon_f, \boldsymbol{k}_\|). \tag{6}$$

Evaluation of the atomic contribution ρ^{atom} for a semi-infinite crystal gives

$$\rho^{atom}(\epsilon_f, \boldsymbol{k}_\|) = \frac{1}{\pi} \text{Im} \left(\text{i}k_1 \sum_{jn} \sum_{\kappa\kappa'\kappa''} \sum_{\mu\mu'\mu''} A_{j\kappa}^{\mu n} D_{\kappa\mu\kappa'\mu'} M_{\kappa'\kappa''}^n D_{\kappa'\mu'\kappa''\mu''}^* A_{j\kappa''}^{*\mu''n} \right). \tag{7}$$

Herein $A_{j\kappa}^{\mu n}$, $D_{\kappa\mu\kappa'\mu'}$ and $M_{\kappa\kappa'\kappa''}^{n}$ denote the spherical coefficients for the final-state wave field, the angular matrix elements and the radial double matrix elements. The summation indices n and j denote the nth atom in the unit cell and the jth layer of the semi-infinite crystal.

Evaluation of the multiple-scattering contributions $\rho^{intra,inter}$, which involve the multiple scattering of the initial state inside and between the layers of the bulk crystal, results in

$$\rho^{intra+inter}(\epsilon_f, \boldsymbol{k}_\parallel) = \frac{1}{\pi} \operatorname{Im}\left(\mathrm{i}k_1 \sum_{jn} \sum_{\kappa\kappa'} \sum_{\mu\mu'} A_{j\kappa}^{\mu n} \tilde{M}_{\kappa\kappa'}^{n} D_{\kappa\mu\kappa'\mu'} (B_{j\kappa'}^{\mu'n} + G_{j\kappa'}^{\mu'n}) \right) \tag{8}$$

with $B_{j\kappa'}^{\mu'n}$ and $G_{j\kappa'}^{\mu'n}$ denoting the spherical coefficients for the intra-layer and inter-layer parts of the initial-state wave field and $\tilde{M}_{\kappa\kappa'}^{n}$ the radial single matrix elements. Final evaluation of the surface contribution gives

$$\rho^{surf}(\boldsymbol{k}_\parallel, \epsilon_f) = -\frac{1}{\pi} \frac{A_z}{2\omega c} \operatorname{Im}\left(\mathrm{e}^{\mathrm{i}\boldsymbol{q}_\parallel \cdot \boldsymbol{c}_{1\parallel}} \sum_{gs} \int_{-\infty}^{c_{1z}} \mathrm{d}z \; \psi_{2gs}(z) \frac{\mathrm{d}V_B}{\mathrm{d}z} \phi_{1gs}(z) \mathrm{e}^{\mathrm{i}q_z z} \right). \tag{9}$$

Herein $\phi_{1gs}(z)$ and $\psi_{2gs}(z)$ denote the regular solutions of the Schrödinger equation for the spin index s for $V_B(z)$ in the range $-\infty < z < c_{1z}$. The value c_{1z} defines the point where the surface potential merges smoothly with the inner potential of the bulk crystal. A_z is the z-component of the amplitude $\boldsymbol{A}_0$ and $\boldsymbol{q}$ is the wavevector of the photon field.

4. Determination of the Fermi surface using ARUPS

The Fermi surface of a metal determines e.g. the electrical conductivity, the heat capacity and the phase stability. The Fermi surface might also influence the reconstruction of surfaces [8–10]. Several methods are able to measure Fermi surfaces, such as those based on the magnetoacoustical, the Shubnikov–de Haas and the de Haas–van Alphen effects [9], positron annihilation, Compton scattering and the Kohn effect [11]. The de Haas–van Alphen method requires a defect-free crystal and is thus problematic when performing measurements on alloys. It gives results on the bulk and is not suited to showing changes arising from the formation of surface alloys. In the case of alloys, ARUPS is a better suited method but with poorer momentum resolution.

To our knowledge this is the first determination of the Fermi surfaces of ruthenium using ARUPS. The Fermi surface of Ru has already been measured using the de Haas–van Alphen method [12–16] and the galvanomagnetic effect [17–19].

Figure 1 shows ARUPS measurements of the Ru(0001) surface near the Fermi energy at different excitation energies. Neighbouring figures show the same experimental data but those on the right-hand side additionally show a spherical coordinate system as distorted by the detection geometry. Interpreting these results, one must keep in mind that they do not depict flat planes in k-space but points of constant energy forming the surface of a sphere in k-space. This implies that $k_\perp$ changes with changing $k_\parallel$. In figure 1(a) a flower pattern of sixfold symmetry can be seen. Using this information, the rotation of the sample around the surface normal was determined to be $13.5° \pm 1.5°$ from the ideal position (meaning that $\overline{\Gamma}\,\overline{K}$ is horizontal). The symmetry points $\overline{K}$ and $\overline{M}$ lie in the region of low intensity. Thus an assignment of the high-intensity regions at polar angles of $30°$ and higher is possible. They stem from neighbouring Brillouin zones.

For comparison, figure 2 shows the Fermi surface determined by de Haas–van Alphen (dHvA) measurements at the height of the Γ point [14]. The good agreement with the data from figure 1(a) is obvious. In table 1 the values for $k_\parallel$ obtained from de Haas–van Alphen measurements, the bandstructure and ARUP spectra are compared and show good agreement.
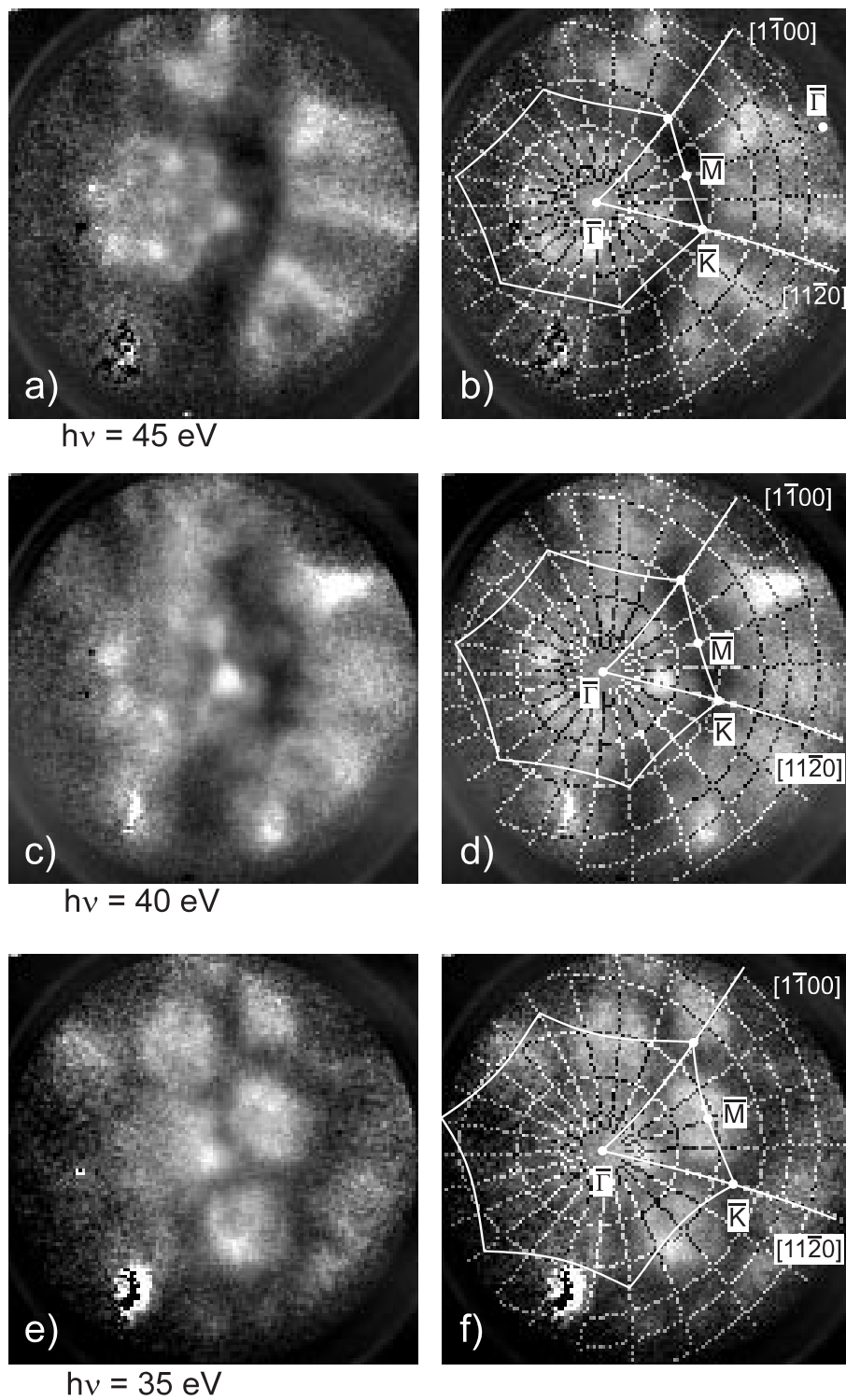
Figure 1. ARUPS measurements of the Ru(0001) surface near the Fermi energy. On the right-hand side a spherical coordinate system is shown additionally. The polar angles highlighted are $10°$, $20°$, $30°$, $40°$, $45°$, $50°$ and the azimuthal angles are depicted every $30°$.
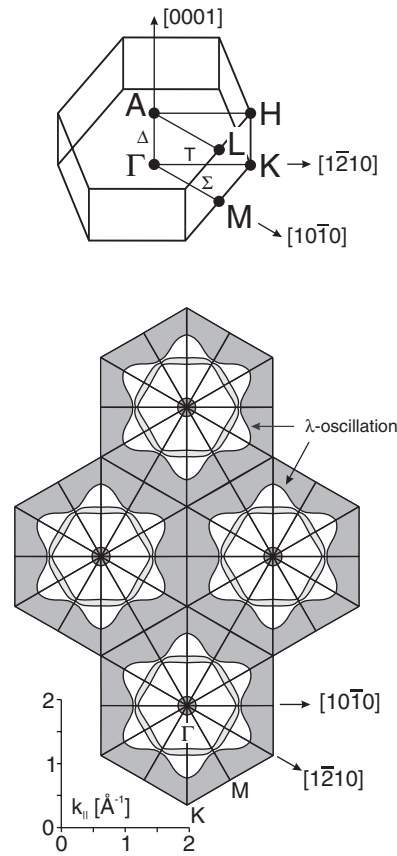
Figure 2. The Fermi surface of Ru(0001) determined by de Haas–van Alphen measurements at the height of the Γ point. The upper part shows the bulk Brillouin zone of Ru.

Table 1.

Method	$k_\parallel$ (ΓK)	$k_\parallel$ (ΓM)
dHvA [13]	1.16 Å^{-1}	0.86 Å^{-1}
Bandstructure (this work)	1.09 Å^{-1}	0.84 Å^{-1}
ARUPS (this work)	1.1 ($\pm$0.1) Å^{-1}	0.8 ($\pm$0.1) Å^{-1}
	($h\nu = 45$ eV)	($h\nu = 45$ eV)

In order to compare the Fermi surface determined by ARUPS with those measured otherwise it is necessary to know all the components of the wavevector $\boldsymbol{k}$. Evaluation of the ARUP spectra demonstrates that the central structure corresponds to the λ-line (see the area marked in figure 2) of the dHvA measurement. As large areas with low intensities are only found in a relatively small $\Delta k_\perp$-interval of approximately 0.6 Å^{-1} (dHvA) the value of $k_\perp$ at 45 eV can be given quite accurately. In the $\overline{\Gamma}\,\overline{\text{K}}$ direction a $k_\perp$-area of 0.4 Å^{-1} is covered on the way from the Γ to the K point. This pins the $k_\perp$-value at the Γ point down to $k_\perp = 3.2$ Å$^{-1} \pm 0.1$ Å^{-1}. With this value the inner potential is evaluated to be $V_0 = -1.6$ eV ± 2.2 eV. In the literature the values range from $V_0 = -2$ eV [20] to $V_0 = 0$ eV [21] with respect to the Fermi energy.

5. Bandstructure of Ru

The electronic structure of Ru has been measured several times in the past using ARUPS. Most of these investigations determined the bandstructure perpendicular to the (0001) surface, because the structure in this direction can be compared with pseudo-fcc structures. Himpsel *et al* [20] studied Ru along the ⟨0001⟩ direction, but found no good agreement with calculated bandstructures available at that time [14, 22]. Since then Bross and Krieter [23] determined the electronic structure of the pseudo-fcc Ru with the augmented-plane-wave method using the potential of Moruzzi *et al* [22], as did Jepsen *et al* [14] applying a relativistic LMTO method and Holzwarth and Chelikowsky [24] using an *ab initio* pseudopotential. This latter calculation as well as the one by Feibelman [25] not only gave the bandstructure along ΓA, but also those along the $\overline{\Gamma}\,\overline{K}$ and $\overline{\Gamma}\,\overline{M}$ directions. Lindroos *et al* computed the Ru bandstructure up to 70 eV along ΓA [21].

5.1. The ΓA direction

Figure 3 depicts the normal-emission spectra for excitation energies from 15 eV to 45 eV. The synchrotron radiation is basically s polarized with respect to the plane determined by the
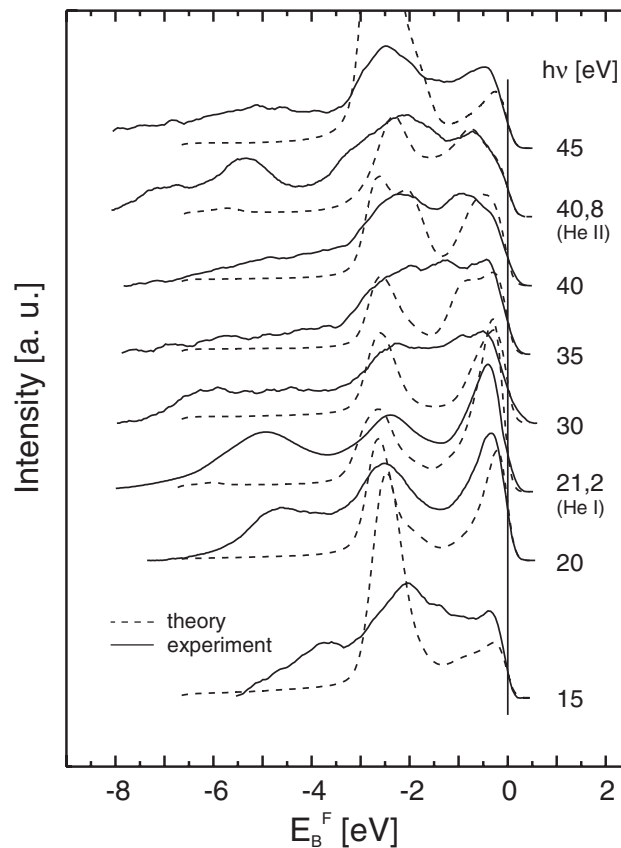

Figure 3. Normal-emission spectra for excitation energies from 15 to 45 eV with basically s-polarized synchrotron radiation and with He I and He II light.

surface normal and the direction of the incoming beam. In addition, spectra obtained in the home laboratory in Bonn with unpolarized He I and He II radiation are presented. All spectra are corrected by background subtraction. For every spectrum we tried to find a correspondence between the measured states and those provided by the relativistic KKR bandstructure shown in figure 4. To this end, photoelectron spectra of the Ru(0001) surface were calculated on the basis of this bandstructure using a one-step model of photoemission described earlier [7]. They are displayed in figure 3 using broken lines. The comparison between the measured and calculated spectra shows generally good agreement. They were normalized at the Fermi energy. The peak positions are nearly always exactly the same and the intensities of the right order of magnitude. The energy resolution of the measured spectra is ⩾350 meV, resulting in peaks not being as distinctly separated as in the calculations, where the experimental resolution was not fully taken into account, for the sake of clarity. Due to the tilt of the sample, the light is not completely s polarized as assumed in the calculations. The state at -1.5 eV ($h\nu = 15$ eV) should not be seen with purely s-polarized light, whereas it should be strong for p-polarized light, as predicted by Lindroos *et al* [21]. The surface resonance at ~ -5 eV ($h\nu = 20$ eV)
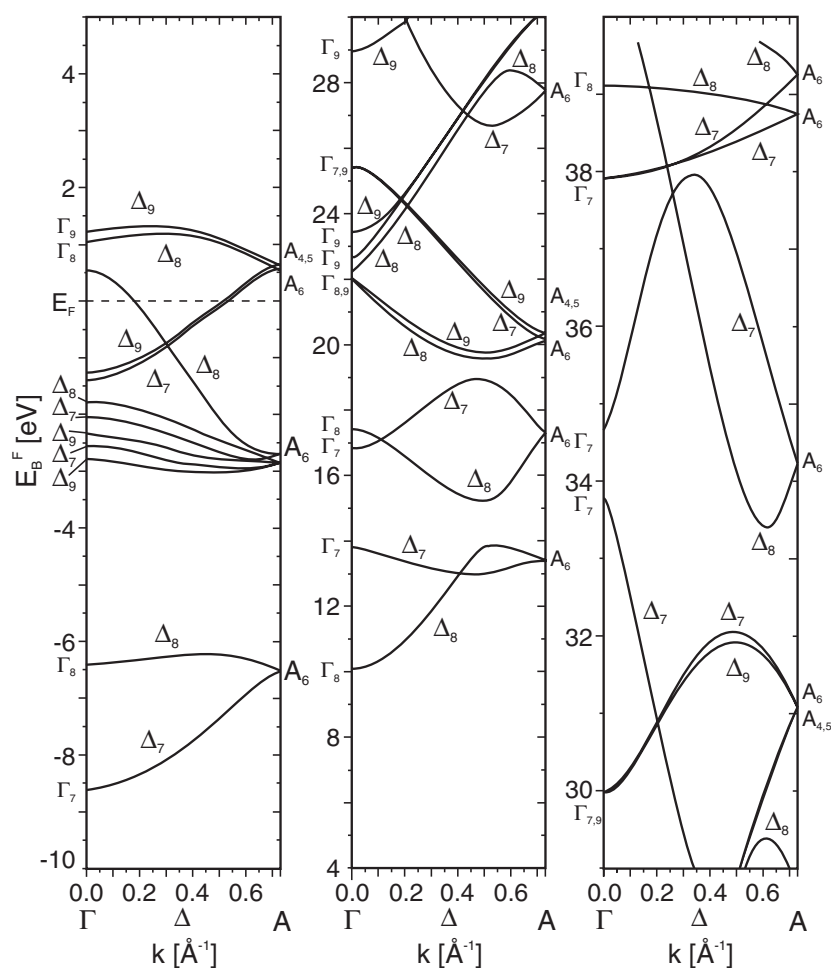

Figure 4. Fully relativistic KKR bandstructure of ruthenium along the ΓA direction.

cannot be reproduced by theory.

In the following the measured peaks are associated with specific bands of the bandstructure in figure 4 using the results of Lindroos *et al*, Holzwarth and Chelikowsky and Himpsel *et al* [20, 21, 24] for the interpretation, keeping in mind that the bandstructure of Lindroos *et al* [21] is nonrelativistic. The state at about ~ -0.5 eV below the Fermi energy is very pronounced up to an excitation energy of 21 eV and then vanishes. Himpsel *et al* as well as Lindroos *et al* [20, 21] attribute this state to the topmost d-like band. In the relativistic bandstructure this is split into two bands denoted by Δ_7 and Δ_9. Part of the intensity may stem from the Δ_8 or Δ_9 states above the Fermi level, which can be registered below the Fermi level due to natural line broadening [21].

The state at a binding energy of ~ -2 eV represents the lower d-like bands Δ_7 and Δ_9 as well as the upper flat sp-like Δ_8 band and the rising band, also with Δ_8 symmetry. In this area, transitions are possible from Δ_7 and Δ_9 to Δ_7 and from Δ_8 and Δ_9 to Δ_8. Unfortunately this does not help with the assignment, because the peaks are too broad for one to be able to decide whether one or more states are concealed under them, and the bands lie very near to one another.

The peak at a binding energy of ~ -4.5 eV at $h\nu = 20$ eV is attributed to the same source as the one at the binding energy of -5 eV obtained after excitation with He I radiation. It can also be excited by electrons [26] and reacts sensitively to adsorbates [27]. We assume that this state is a surface state.

The maximum of the structure at a binding energy of -5.3 eV occurring at excitation energies of 40.8 eV and 45 eV is nearly constant in energy. This state lies in the band gap between the lower Δ_7, Δ_8 bands and the closely lying upper Δ_7, Δ_8 and Δ_9 bands. We therefore assume this to be a surface state.

Himpsel *et al* and Lindroos *et al* [20, 21] both describe a state at a binding energy of -7.3 eV only arising in a small interval of photon energies between 37 and 40 eV. It is also present in the spectrum at an excitation energy of 40.8 eV (figure 3). Himpsel *et al* attribute this peak to a transition at $\Gamma(0002)$ and exclude the possibility of a resonance with the 4p level of ruthenium. This resonance should only occur at 43 to 46 eV [20]. A possible initial state could be the steep band at $k = 0.22$ Å^{-1}. But the steepness should lead to a lower intensity and we do not find an adequate final state. We thus favour the explanation in terms of the resonance.

5.2. The $\overline{\Gamma}\,\overline{K}$ and $\overline{\Gamma}\,\overline{M}$ directions of the Ru Brillouin zone

Off-normal ARUPS measurements allow one to determine the properties of the high-symmetry directions not available with normal emission. In the following we show ARUP spectra along $\overline{\Gamma}\,\overline{K}$ and $\overline{\Gamma}\,\overline{M}$ directions for excitation energies of 45, 40 and 20 eV as well as a measured and a calculated projected bandstructure and comparisons between measured and calculated data.

Using the disappearance angle/appearance angle method proposed by Christensen [28] the limits of the Brillouin zone are determined. In this method, irregularities in the energy distribution curves are seen as arising from band splitting at the boundaries of the Brillouin zone. The location of the boundaries is illustrated by the spectra obtained at an excitation energy of 45 eV.

The HK boundary is parallel to the ΓA line and crosses the K and the H point. In figure 5 on the left-hand side, depicting spectra in the $\overline{\Gamma}\,\overline{K}$ direction, anomalies show up at the points 5, 6, 7 and 8. In the vicinity of point 5 ($\Theta_{ext} \sim 27°$, $E_B^F \sim -1.25$ eV) a sudden significant increase in the intensity occurs and a local minimum of the binding energy is discernible at this angle. At $\Theta_{ext} \sim 22.7°$ and $E_B^F \sim -2.5$ eV a new structure (6) is forming. The intensity variation and the shift of the peak at $E_B^F \sim -4$ eV (denoted by 8) are particularly noticeable. Here a
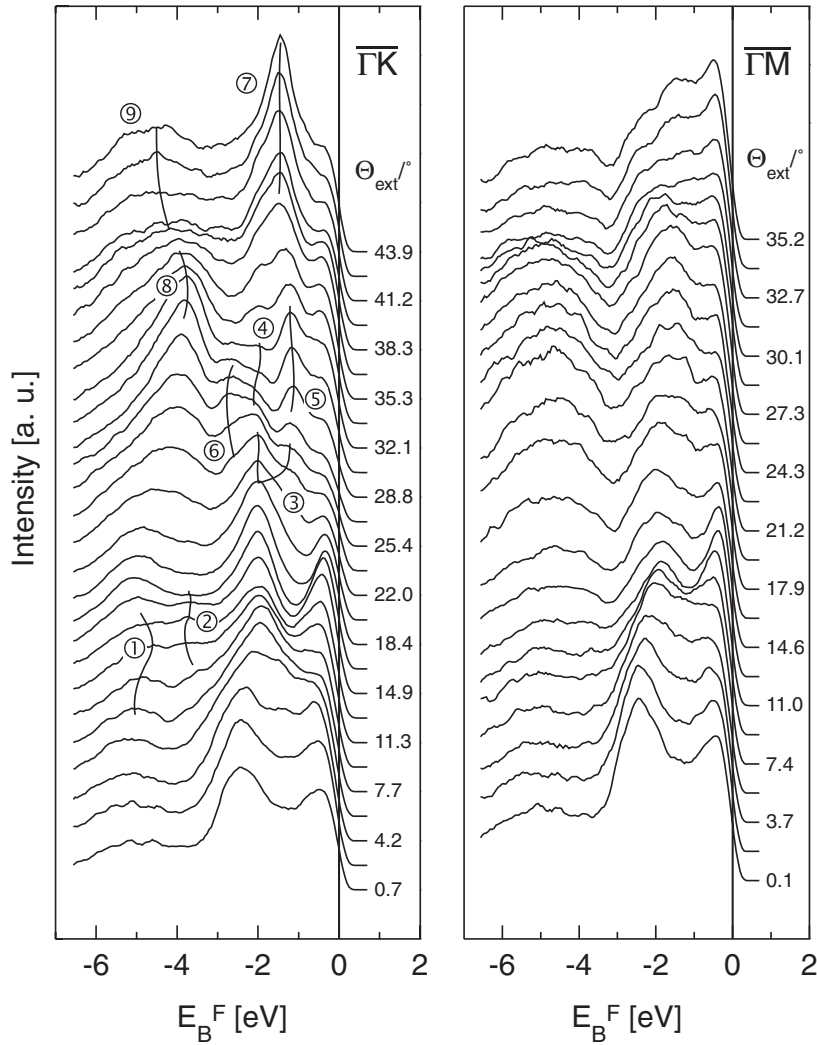
Figure 5. ARUP spectra along the $\overline{\Gamma}\,\overline{K}$ and $\overline{\Gamma}\,\overline{M}$ directions ($h\nu = 45$ eV).

marked intensity increase with increasing emission angle coincides with the peak maximum moving to lower binding energies. Maximum intensity and minimal binding energy are reached at $\Theta_{ext} \sim 30°$. With further increasing emission angle, the intensity decreases fast and the binding energy shifts towards higher values.

The calculations for $k_{\parallel}$ for the above-mentioned points leads to $k_{\parallel} = 1.5$ Å$^{-1} \pm 0.1$ Å^{-1}. This corresponds to the transition of the bands through the ΓH line expected from calculations at 1.55 Å^{-1}.

The ΓK line lies parallel to the (0001) plane. The projection of this line onto the (0001) plane is at the same time the AH boundary of two neighbouring Brillouin zones. The bands going through the points 1 and 2 have minimal or maximum binding energy. According to the projected bandstructure, the points 1, 2 and 3 cannot be attributed to the crossing of the AH boundary. Assuming an inner potential of -1.6 eV, a $k_{\perp}$-value for the above-mentioned points of $k_{\perp} = 2.92$ (± 0.2) Å^{-1} can be determined. This corresponds to the $k_{\perp}$-value of the ΓK line

of the third Brillouin zone. The increase in intensity at a binding energy of ~ -1.2 eV for large emission angles ($\Theta \geqslant 40°$) is due to the band crossing the HL symmetry line at $k_\perp = 2.19$ Å^{-1} which separates the second and the third Brillouin zones. The HL line is the continuation of the AH line into the next Brillouin zone.

The measured projected bandstructure (see figure 6, for excitation energy 45 eV) was obtained by displaying all energy distribution curves in a high-symmetry direction side by side and encoding the intensities in a grey-tone scale. Each vertical line gives the intensity of photoelectrons at angles Θ_{ext}, Φ_{ext} for different binding energies. Taking the energy distributions along a high-symmetry direction leaves the azimuthal angle Φ_{ext} constant, while Θ_{ext} is being changed. From the binding energy, the excitation energy and the polar angle $k_\parallel$ can be calculated. A corresponding scale is found on the abscissa. To obtain as high a contrast as possible, the intensity of each energy distribution curve was multiplied by a factor such that the highest intensity is displayed with the maximum brightness. The curves thus obtained are no longer suitable for quantitative analysis, since this factor is different for each of them. The grey-tone picture is provided to give a visual impression of the projected bandstructure.
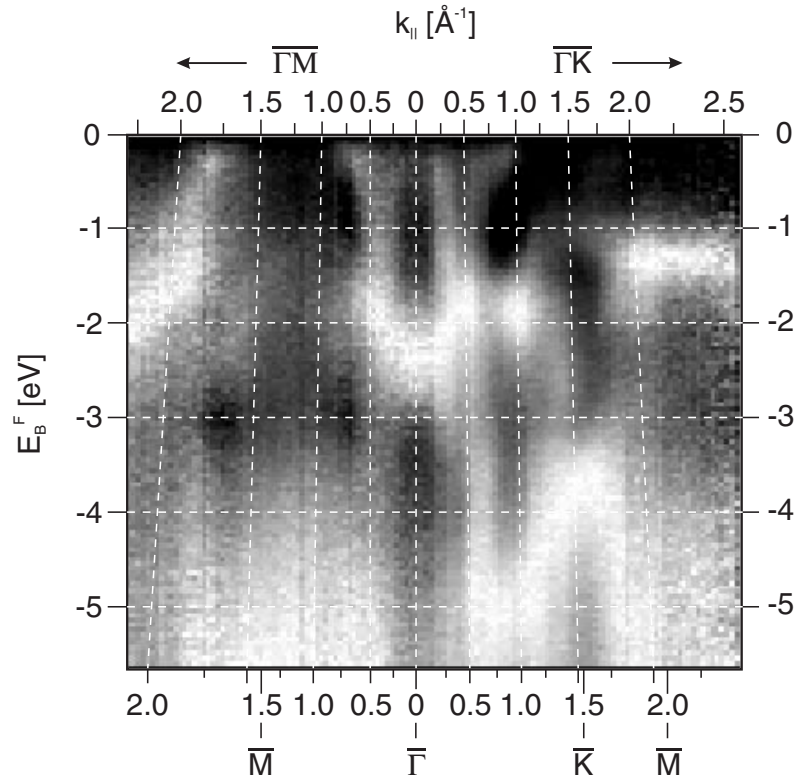

Figure 6. A grey-tone picture of the projected bandstructure ($h\nu = 45$ eV).

When comparing the grey-tone picture obtained at an excitation energy of 45 eV (figure 6) with the projected bandstructure [24] (figure 7) some structures can be recognized, e.g. the band gap in the binding energy range -3 eV $\geqslant E_B^F \geqslant -6$ eV around the $\overline{\Gamma}$ point as well as a gap around $k_\parallel \sim 1$ Å^{-1} at the Fermi energy. One can also discern the surface states in the band gap at the $\overline{K}$ point and a binding energy of ~ -2 eV.

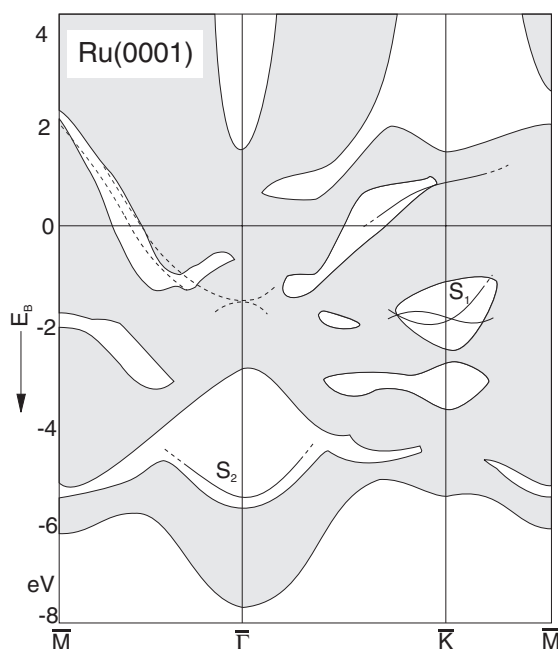In the grey-tone display, the Brillouin zone boundary at the $\overline{K}$ point can be seen very

Figure 7. Projected bandstructure of Ru(0001) [24].

distinctly as a parabola-like structure in the range -3 eV $\geqslant E_B^F \geqslant -5.5$ eV, whose maximal binding energy is at $k_\parallel = 1.5$ Å^{-1}. This corresponds to the point 8 in figure 5 and is attributed to the crossing of the KH line. Also, the width of the Fermi surface can be estimated along the $\overline{\Gamma}\,\overline{K}$ and $\overline{\Gamma}\,\overline{M}$ directions.

At other excitation energies one can also see the Brillouin zone boundaries. We will not dwell on this subject here, but rather present comparisons of measured and calculated spectra, beginning with an excitation energy of 40 eV—see figure 8, where the solid and broken lines depict the measured and calculated data, respectively. The curves are labelled with their emission angles. The peak positions are well reproduced, with the exception of the spectrum at $\Theta = 30°$ in the $\overline{\Gamma}\,\overline{M}$ direction, where the intensity at E_B^F is markedly too high. We attribute this to higher uncertainties in the calculations at higher angles or to the influence of the p polarization arising from the tilt of the crystal which is not taken into account in the calculations.

A similar comparison for an excitation energy of 20 eV is exhibited in figure 9. Here one also sees a good agreement between measured and calculated data with the exception of the surface resonance at ~-4.5 eV which is not reproduced in the calculation.

6. Surface states on Ru(0001)

The projected bandstructure of Holzwarth and Chelikowsky [24] (see figure 7) predicts a band gap between the s and d bands in the vicinity of the $\overline{\Gamma}$ point in the binding energy range from -3 eV to -5.7 eV. A surface state exists in this gap which follows the upper s band (lower band-gap edge) and has a binding energy of -5.5 eV at $\overline{\Gamma}$. It is denoted as S_2 and is located in the first two layers. In addition, Holzwarth and Chelikowsky find two other sets of surface bands in the d-band complex. At -1.5 eV, two doubly degenerate states exist at $\overline{\Gamma}$ which extend
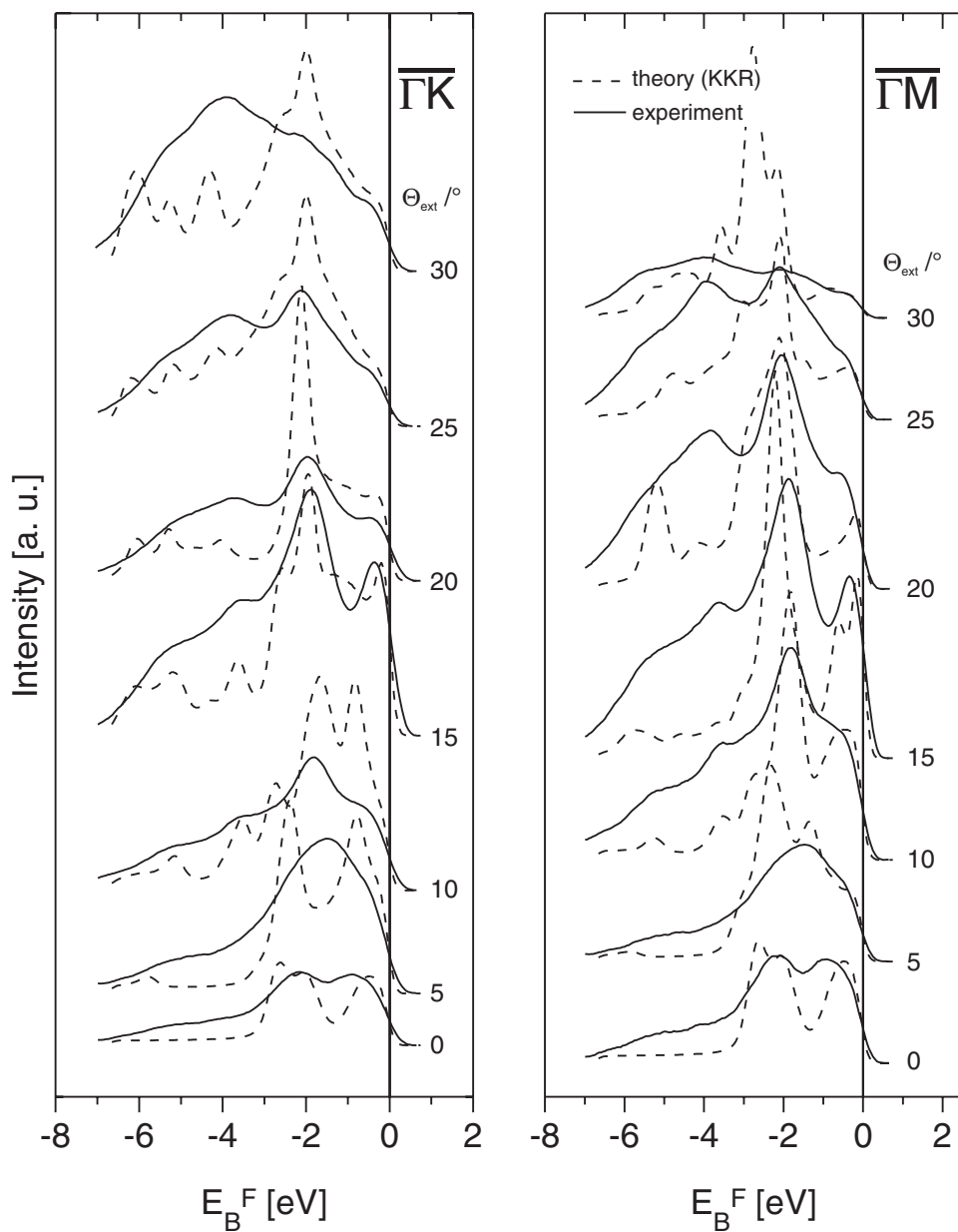
Figure 8. Comparison of measured (solid lines) and calculated (broken lines) spectra for an excitation energy of 40 eV.

through a very small region of the Brillouin zone. In the $\overline{\Gamma}\overline{M}$ direction one surface state and three surface resonances are found, which are highly concentrated in the surface layer. Since these states extend only through a small region of the Brillouin zone, they are not expected to be visible experimentally. In the higher-energy gap near the $\overline{K}$ point, two surface states exist. They extend throughout most of the gap and are degenerate at $\overline{K}$. They should be easily detected experimentally [24].
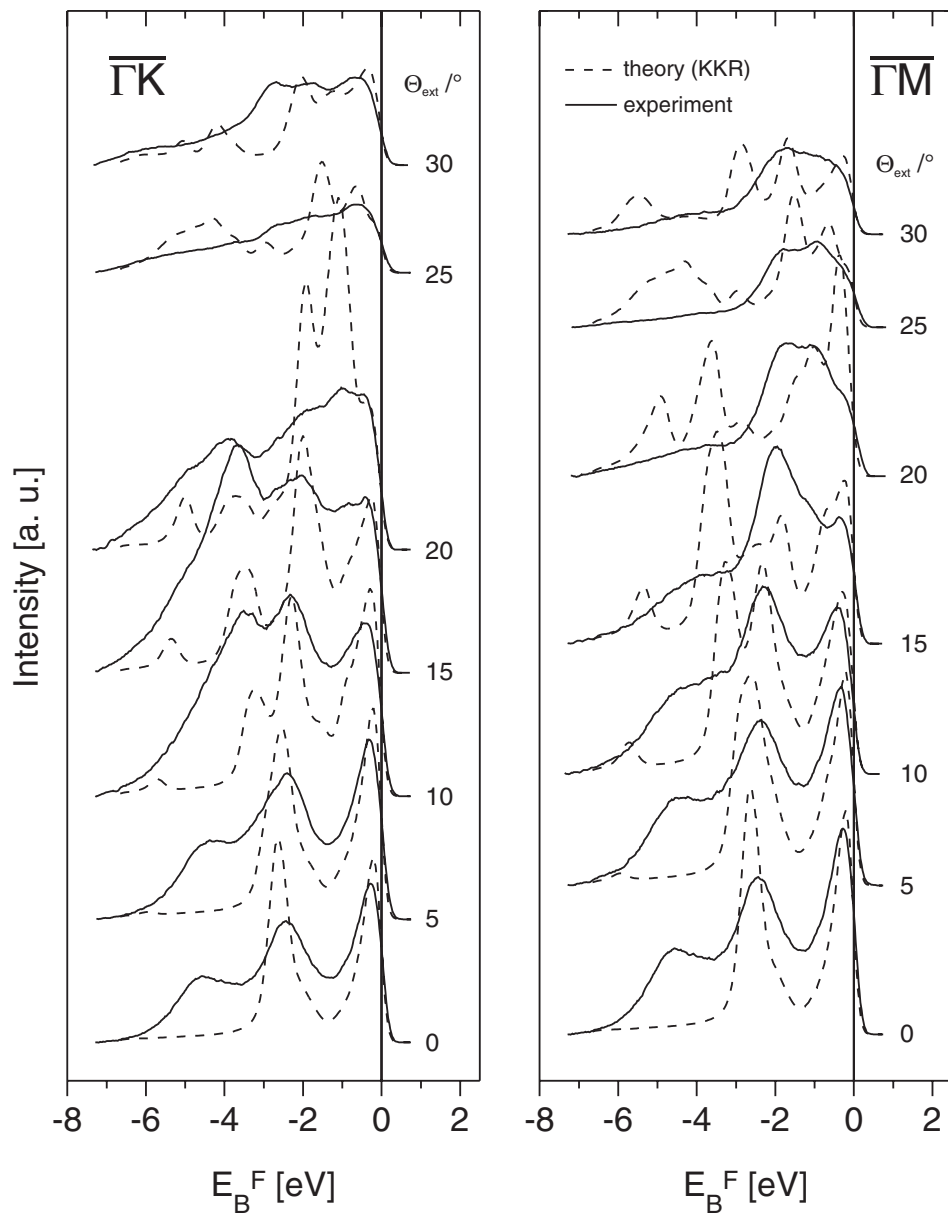
Figure 9. Comparison of measured (solid lines) and calculated (broken lines) spectra for an excitation energy of 20 eV.

The surface resonance calculated to lie at approximately -5.5 eV (the $\overline{\Gamma}$ point) is observed experimentally at -4.5 eV as can be seen in figure 10, where the experimentally observed surface states at different excitation energies are shown together with the calculated ones [24]. By way of contrast, we find a very good agreement as regards the position of the surface state denoted by S_1 (see figure 10).

Since surface states as well as resonances react very sensitively to contaminations, the existence of these states leads us to the conclusion that the surface was well defined and clean.
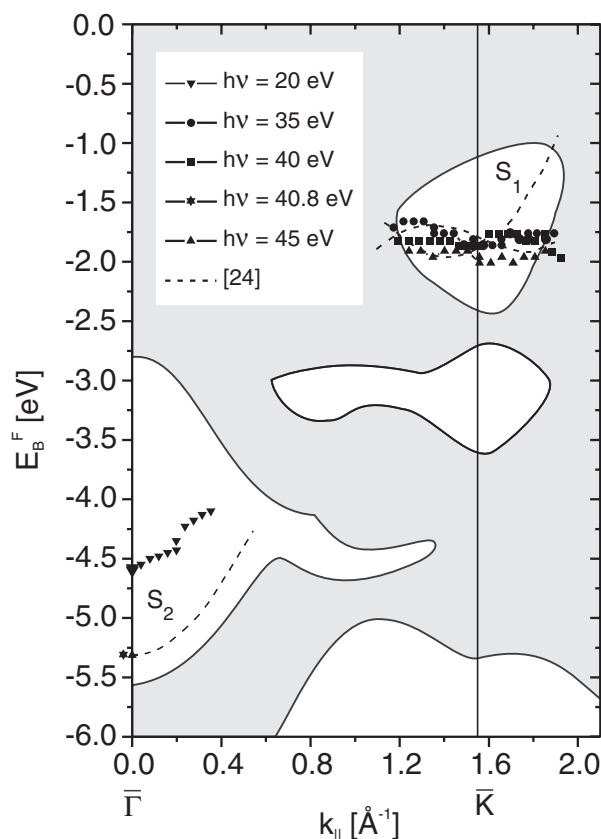
Figure 10. Comparison of measured and calculated surface states [24].

7. Summary

It was possible to determine for the first time the Fermi surface of ruthenium at different excitation energies using ARUPS. The comparison with de Haas–van Alphen measurements showed good agreement. Due to the compact structure of the Fermi surface, the crystallographic directions could be clearly assigned and an inner potential of $V_0 = -1.6$ eV was determined. From the photoemission curves in the $\overline{\Gamma}\,\overline{M}$ and $\overline{\Gamma}\,\overline{K}$ directions, the Brillouin zone boundaries could be provided, using the appearance/disappearance method. It was demonstrated that with photon energies in the range of $h\nu = 20$ eV to 45 eV the third and part of the second Brillouin zone could be mapped. It was also possible to verify the surface states. The spectra calculated on the basis of the one-step model of photoemission generally displayed a very good agreement with the measured ones as regards the energetic position as well as the intensity.

References

[1] Rieger D, Schnell R-D, Steinmann W and Saile V 1983 *Nucl. Instrum. Methods* **208** 777
[2] Eastman D E, Donelon J J, Hien N C and Himpsel F J 1980 *Nucl. Instrum. Methods* **172** 327
[3] Pistitsch C 1993 *Diploma Thesis* University of München
     Thomann U, Rangelov G and Fauster Th 1995 *Surf. Sci.* **331–333** 1283

[4] *Landolt–Börnstein New Series* 1984 Group III, vol 13c (Heidelberg: Springer)
[5] Wandelt K, Hulse J and Küppers J 1981 *Surf. Sci.* **104** 212
[6] Holleman A F and Wiberg W 1995 *Lehrbuch der anorganischen Chemie* (Berlin: de Gruyter)
[7] Braun J 1990 *Rep. Prog. Phys.* **59** 1267
[8] Jeong K, Gaylord R H and Kevan S D 1989 *Phys. Rev.* B **39** 2973
[9] Gaylord R H, Jeong K H and Kevan S D 1989 *Phys. Rev. Lett.* **62** 2036
[10] Kevan S D 1990 *Phys. Scr.* T **31** 32
[11] Kittel C 1983 *Einführung in die Festkörperphysik* (München: Oldenbourg)
[12] Coleridge P T 1966 *Phys. Rev. Lett.* **22** 367
[13] Coleridge P T 1969 *J. Low Temp. Phys.* **1** 577
[14] Jepsen O, Andersen O K and Mackintosh A R 1975 *Phys. Rev.* B **12** 3084
[15] Alekseevskii N E, Blinski M and Nizhankouskii V I 1978 *J. Low Temp. Phys.* **30** 599
[16] Alekseyev E S, Ventsel V A, Voronov O A, Likhter A I and Magnitskaya M V 1979 *Sov. Phys.–JETP* **49** 110
[17] Botin G A, Volkenstein N V, Novoselov V D and Startzev V E 1972 *Fiz. Met. Metallov.* **33** 740
[18] Volkenstein N V, Dyakina V P, Startzev V E, Azhazha V M and Kovtun G P 1981 *Fiz. Met. Metallov.* **38** 718
[19] Alekseevskii N E, Berthel K H, Dubrovin A V, Nizhankouskii V I and Urai L 1973 *Pis. Zh. Eksp. Teor. Fiz.* **18** 277
[20] Himpsel F J, Christman K, Heimann P and Eastman D E 1981 *Phys. Rev.* B **23** 2548
[21] Lindroos M, Hofmann P and Menzel D 1986 *Phys. Rev.* B **33** 6798
[22] Moruzzi V L, Janak J F and Williams A R 1978 *Calculated Electronic Properties of Metals* (New York: Pergamon)
[23] Bross H and Krieter F 1984 *Diploma Thesis* University of Munich
[24] Holzwarth N A W and Chelikowsky J R 1985 *Solid State Commun.* **53** 171
[25] Feibelman P J 1982 *Phys. Rev.* B **26** 5347
[26] Hesse R, Staib P and Menzel D 1979 *Appl. Phys.* **18** 227
[27] Hofmann P and Menzel D 1979 *Surf. Sci.* **88** 65
[28] Christensen N E 1981 *Solid State Commun.* **38** 309